Soil Dynamics and Earthquake Engineering 150 (2021) 106909

Contents lists available at ScienceDirect

Soil Dynamics and Earthquake Engineering

journal homepage: www.elsevier.com/locate/soildyn

Seismic performance and fragility analysis of power distribution concrete poles

Amir Ghahremani Baghmisheh, Mojtaba Mahsuli *

Center for Infrastructure Sustainability and Resilience Research, Department of Civil Engineering, Sharif University of Technology, Tehran, Iran

ARTICLE INFO

Keywords:
Power pole
Damage fragility
Collapse risk
Reinforced concrete
Infrastructure resilience

ABSTRACT

This paper proposes probabilistic damage and collapse models for reinforced concrete poles in electric power distribution networks and investigates the damage and collapse pattern of poles under earthquake excitations. To this end, detailed finite element models of the H-type reinforced concrete poles are developed and verified using past experimental studies as well as the observed damage in previous earthquakes. The models are then subjected to nonlinear static analyses to study the effect of the loading pattern, loading direction, concrete strength, and failure criteria on the capacity and the collapse pattern of the pole. Next, incremental dynamic analysis is carried out to investigate the sensitivity of the seismic response and collapse pattern of the pole to the direction of ground motion, record-to-record variability, and concrete strength. The results show that the damage pattern under static pull tests, which are the only type of the test conducted on such poles, poorly represent the seismic collapse pattern of the pole. The results also reveal that the most vulnerable segment of the pole is the first 0.5 m of the pole above the ground, which can guide the future retrofit strategies. The results of the incremental dynamic analysis are subsequently employed to develop damage and collapse fragility models for 9, 12, and 15 m long poles using the maximum likelihood method. The analysis accounts for the uncertainty not only in the ground motion but also in the material properties of poles. The proposed models make it possible to account for the damage incurred by the power distribution lines in the seismic risk analysis of the power distribution networks as well as the seismic resilience analysis of electrified communities.

1. Introduction

This paper evaluates the seismic vulnerability and damage patterns of power distribution concrete poles and proposes damage and collapse fragility models to be utilized in risk and resilience analysis of power distribution networks. Poles structurally support cables that distribute electricity. The seismic performance of poles significantly affects the performance and serviceability of the power network following an earthquake. Poles are manufactured with different materials that include wood, steel and reinforced concrete. Construction of wood poles has raised environmental concerns recently, and their durability is under question [1]. Therefore, concrete poles are more cost-effective when the life cycle costs, including those of maintenance, are taken into account [2]. Moreover, steel poles and towers cost twice the concrete poles to manufacture [1]. As such, concrete poles have been the dominant type of power distribution poles manufactured over the last two decades and are amongst the most frequent components of the electric power infrastructure.

The performance of poles can strongly be affected by natural hazards such as windstorms and earthquakes. The performance of wood poles is more affected by windstorms due to their light weight. The performance of concrete poles is, however, more affected by earthquakes due to their high self-weight. Numerous damages of the concrete pole were reported in previous earthquakes [3]. For instance, 40% of such poles were no longer functional after Bam 2003, Iran earthquake [4]. The failure of the pole causes power outage, which in turn results in significant economic losses due to business interruption. Moreover, the power outage of critical facilities such as hospitals or emergency management facilities not only increases the social losses due to higher fatalities, but it also interrupts the emergency response and recovery. This highlights the importance of investigating the vulnerability of poles and modeling their damage and collapse in regional risk and community resilience assessments [5–9]. Such analyses are paramount for optimal allocation of limited resources to risk mitigation and resilience enhancement policies and their results are significantly affected by the proper modeling of damage to infrastructure components. Even though the damage

* Corresponding author.
E-mail addresses: amir.ghahremani95@student.sharif.edu (A.G. Baghmisheh), mahsuli@sharif.edu (M. Mahsuli).

https://doi.org/10.1016/j.soildyn.2021.106909
Received 16 November 2020; Received in revised form 26 June 2021; Accepted 21 July 2021
Available online 5 August 2021

modeling of power substations and their components is well-studied [10–18], such models are unavailable in the literature for power poles, a gap that is addressed in the present paper. The literature on power poles focuses merely on the evaluation of the structural capacity of poles under static loading in laboratory experiments and numerical simulations. The end result of these studies is the force-displacement curves in flexure. In contrast, the present paper conducts incremental dynamic analysis (IDA) [19] on the detailed finite element (FE) models of concrete poles to produce seismic damage and collapse fragility models.

Several studies conducted experimental tests on concrete poles under static loadings. Henin et al. [2] proposed a novel prestressed concrete pole reinforced by glass-fiber reinforced polymer (GFRP) in order to reduce corrosion and life cycle cost of poles and conducted monotonic static tests to calculate the flexural, shear, and deflection capacity of such poles. The test resulted in the force-displacement curves in three stages: linear elastic, nonlinear with softening, and sudden reduction in load-bearing capacity. Saafi and Asa [20] conducted field pull tests on deteriorated wood poles strengthened by fiber-reinforced polymer (FRP) layers. The test revealed that FRP wraps markedly improve the loading capacity. Vivek et al. [21] subjected tapered concrete poles embedded in various footing to static loading and unloading sequences to determine the loading capacity of the poles. They found that using concrete or stone-grouted footings does not alter the load-bearing capacity or the force-displacement relationship. Kilukas et al. [22] evaluated the performance of concrete poles that were under service for more than 30 years and had experienced different types of deterioration. They found that deterioration reduced the flexural capacity of poles by 35%. Argo [23] investigated the capacity of H-type concrete poles in a full-scale monotonic test.

The static tests conducted on concrete poles have yielded insights on their damage and failure patterns. In a test carried out by Henin et al. [2], failure started by the yielding of vertical bars in tension followed by the crushing of the concrete on the compression side. The failure occurred near the ground level where the flexural moment was maximum. For the poles tested by Vivek et al. [21], a significant number of fine transverse cracks along the pole height were observed in the tension face of the pole. Kilukas et al. [22] tests on deteriorated concrete poles revealed that collapse was mainly caused by the failure of longitudinal reinforcement. In some cases, the collapse was associated with crushing of the concrete in compression. For all specimens tested by Argo [23], cracks formed mainly on the near ground portion of the pole and penetrated to reach the longitudinal reinforcement. The collapse was accompanied by the spalling of concrete in the compression face. The static nature of loading in these tests limits the generalizability of the results to earthquake excitations.

In addition to experimental studies, numerical methods have been applied to the study of the performance of power poles. Saboori and Khalili [24] developed an FE model for tapered fiber-reinforced poles and carried out a dynamic transient analysis to investigate the effects of cable tension and vehicle impact. Vivek et al. [21] carried out a sensitivity analysis on a concrete pole modeled numerically to investigate the effect of soil parameters on the response of the pole, taking into account soil-structure interaction effects. Zeynalian and Khorasgani [25] investigated the effects of harsh weather conditions on a 7-span distribution line by developing FE models for H-type concrete poles and cables. They conducted a nonlinear pushover analysis to detect the weakest part of the distribution line.

The present paper is the first to investigate the performance and the damage pattern of concrete poles under earthquake excitations. The results are then employed to propose novel probabilistic damage models to be used in seismic risk and resilience analysis of power distribution networks. To this end, detailed finite element models of H-type reinforced concrete poles are constructed. The model is then validated using the results of previous experimental studies and the observed damage in prior earthquakes. The model is then subjected to parametric nonlinear static analyses that yields the capacity curve of the pole to investigate the effect of various parameters on the capacity and the collapse pattern of the pole. Next, the model is subjected to incremental dynamic analysis to compute the probability distribution of the engineering demand parameters that govern the damage and collapse of the pole, i.e., the maximum drift and the residual drift of the pole, given various levels of the spectral acceleration at the fundamental period of vibration. The IDA incorporates both the variability of ground motion and the uncertainty in the material properties of poles. Finally, the results of IDA are employed to propose damage and collapse fragility models using the maximum likelihood procedure. These models are immediately applicable in seismic risk analysis of power distribution networks and seismic resilience assessment of electrified communities [5,26–31]. The present paper also yields insights into the most vulnerable area along the height of the pole that can guide efforts on more seismic resistant design as well as cost-effective retrofit strategies of concrete poles.

Table 1
Characteristics of power poles.

Property	Value
F_y transverse rebar	340 MPa
F_y longitudinal rebar	400 MPa
F_c concrete	22 MPa
Steel elastic modulus	210 GPa
Concrete elastic modulus	19.3 GPa

2. Modeling

The first step in this research is to develop a detailed three-dimensional finite element model of H-type concrete poles. ABAQUS [32] is employed here to develop the model. This section presents the modeling details including the geometry, material properties, and element and boundary conditions. The failure criteria of the pole are presented next followed by the validation of the model with real-world observations from past earthquake as well as the results of experimental studies in the literature.

2.1. Geometry

Concrete power poles are usually constructed with a decreasing section area along the height in order to reduce the total weight. The H-type poles contain concavities along the length to further reduce the weight. This complex configuration makes a precise modeling of the pole challenging. As such, past studies have all neglected the details of concavities in favor of a simpler model; see, for instance, Refs. [3,25]. This may markedly affect the damage pattern and the prediction quality of the ensuing fragility models. Thus, the present study precisely models the details of the geometry of the pole, including those of the concavities.

Considered poles are 9 m, 12 m, and 15 m high, which form the majority of the concrete poles in the distribution network. Trapezoidal concavities are distributed on two faces of poles with a spacing of 750 mm along the height. Table 1 shows the characteristics of poles, and Fig. 1 illustrates the geometric details along with the cross section at different locations along the height. Four main AIII bars with a diameter of 16 mm placed at corners of the section are continued in the whole length; however, other ones are trimmed at different distances from the bottom. The transverse AII bars with a diameter of 6 mm are evenly spaced with a spacing of 25 mm. The configuration of the modeled 12 m-long pole in conjunction with the placement of longitudinal and transverse bars are demonstrated in Fig. 2. The model for the 12 m pole yields a concrete volume of 0.67 m^3, which concurs with the real-world volume of 0.65 m^3 provided by the manufacturer.

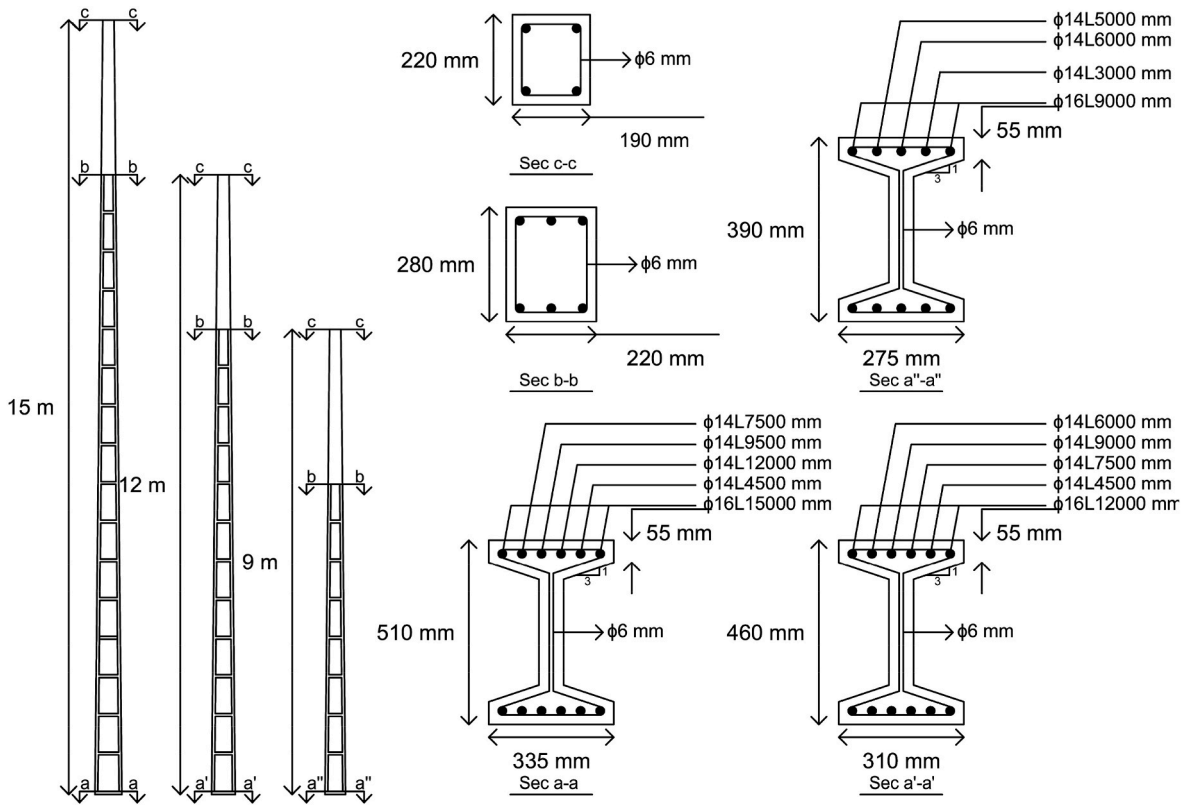

Fig. 1. Longitudinal view and cross-section details of power poles.

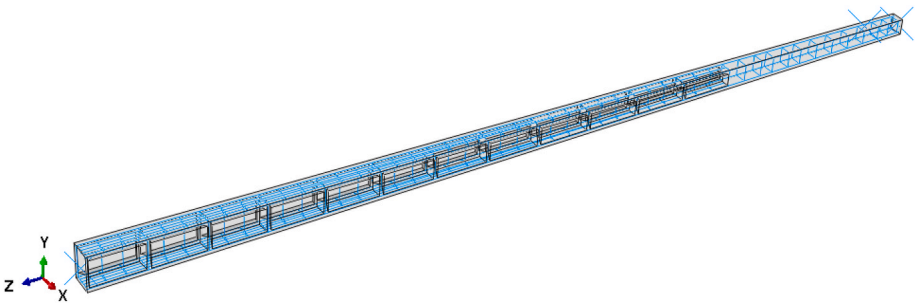

Fig. 2. Three-dimensional geometry of the 12 m-long pole and the embedded steel bars.

Table 2
Plastic parameters of the CDP model.

Parameter	Value
Dilation angle	36
Eccentricity	0.1
Ratio of initial biaxial compressive strength to initial uniaxial compressive strength	1.16
Shape factor for yield surface	0.67
Viscosity parameter	0

2.2. Material properties

This section introduces the material properties for the concrete and the steel used in manufacturing the power poles. First, the modeling of the material properties for concrete is addressed. ABAQUS offers three material models for concrete comprising the brittle cracking model, the smeared cracking model, and the concrete damage plasticity model. In the brittle cracking model, a linear elastic behavior is assumed for concrete in the compression, which is appropriate for modeling plain concrete. On the other hand, the smeared cracking model is commonly employed for structures under monotonic loading [33]. Finally, the concrete damage plasticity (CDP) model has been proposed by Lee and Fenves [34] for reinforced concrete structures subjected to static, cyclic, and dynamic loading. Since the damage of the reinforced concrete pole is evaluated here under static and earthquake loadings, the CDP model is employed to simulate the plastic and damage behavior.

Defining plastic behavior in the CDP model requires five plastic parameters and two sets of stress-strain relationships for compression and tension. Plastic parameters listed in Table 2 define the plastic flow, yield surface function, and viscosity of the material. These parameters are adjusted based on the common practice in modeling normal strength reinforced concrete [35–38]. A detailed description of the plastic flow and the yield function of the CDP model was provided in previous studies [35,39]. For the stress-strain relationship of concrete in compression, Hognestad's model [40] presented in the following equations is adopted:

$$f_c = f_c' \left[\frac{2\varepsilon_c}{\varepsilon_o} - \left(\frac{\varepsilon_c}{\varepsilon_o} \right)^2 \right] \quad (1)$$

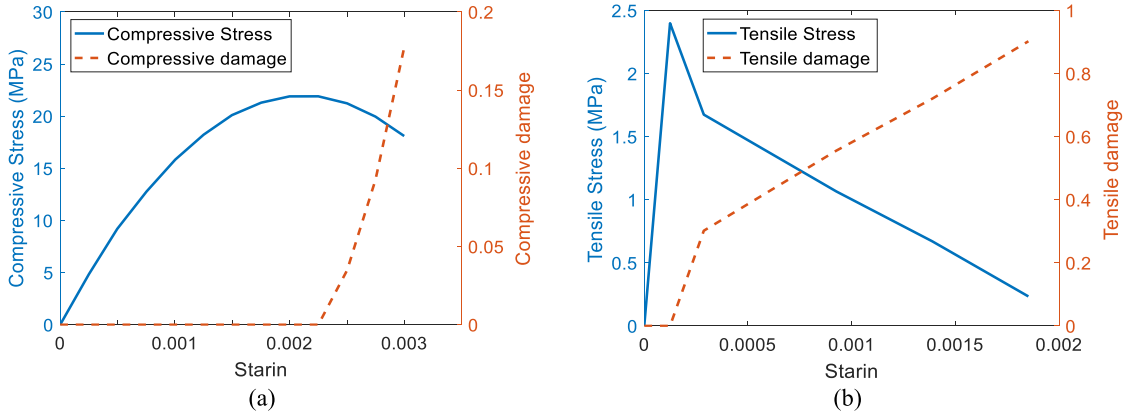

Fig. 3. (a) Compressive and (b) tensile stress-strain relationships for concrete.

$$\varepsilon_o = \frac{2f_c'}{E_c} \tag{2}$$

where f_c is the compressive concrete strength at any strain, ε_c, f_c' is the maximum concrete strength, ε_o is the strain associated with the stress of f_c', and E_c is the elastic modulus, computed using the equation $E_c = 3925\sqrt{f_c'}$ in MPa units [41]. Fig. 3a shows the stress-strain curve of the concrete in compression obtained through the abovementioned equations. For the tensile behavior of concrete, the multilinear model suggested by Wahalathantri et al. [42] is adopted. This model assumes a linear elastic behavior until the fracture stress, f_t, followed by a linear softening behavior up to the ultimate strain to consider the cracking of the concrete. The fracture stress is assumed as 10% of the maximum compressive strength. Fig. 3b demonstrates the concrete stress-strain relationship in tension.

In addition to plastic properties, damage data should be introduced into the CDP model to characterize stiffness degradation effects and the failure of the material. Two damage parameters are used for this purpose in the CDP model, and are defined as follows:

$$d_c = 1 - \frac{\sigma_c}{f_c'} \tag{3}$$

$$d_t = 1 - \frac{\sigma_t}{f_t} \tag{4}$$

where d_c and d_t are respectively damage parameters in compression and tension, σ_c and σ_t are respectively the stress in compression and tension, and f_t is the tensile fracture stress of concrete. Damage parameters range between zero and unity to describe undamaged and fully-damaged states, respectively. Variations of these parameters versus strain are depicted in Fig. 3.

Finally, plastic strains, ε_c^{pl} and ε_t^{pl}, are computed by following equations:

$$\varepsilon_c^{pl} = \varepsilon_c^{in} - \frac{d_c}{(1-d_c)}\frac{\sigma_c}{E_o} \tag{5}$$

$$\varepsilon_t^{pl} = \varepsilon_t^{ck} - \frac{d_t}{(1-d_t)}\frac{\sigma_t}{E_o} \tag{6}$$

where inelastic strain, ε_c^{in}, and cracking strain, ε_t^{ck}, are derived by subtracting the elastic strain of undamaged concrete (ε_{oc}^{el} and ε_{ot}^{el}) from the total strain (ε_c and ε_t), as follows:

$$\varepsilon_c^{in} = \varepsilon_c - \varepsilon_{oc}^{el} = \varepsilon_c - \frac{\sigma_c}{E_c} \tag{7}$$

$$\varepsilon_t^{ck} = \varepsilon_t - \varepsilon_{ot}^{el} = \varepsilon_t - \frac{\sigma_t}{E_c} \tag{8}$$

For longitudinal and transverse bars, an elastic, perfectly plastic stress-strain relationship is adopted. Properties of bars including yield stress and modulus of elasticity were previously listed in Table 1.

To account for the uncertainty of material properties in the fragility analysis, the compressive strength of concrete and the yield strength of reinforcing bars are modeled by random variables. The mean values of these variables are 22 and 400 MPa, respectively, obtained from the experimental study by Zeynalian and Khorasgani [25]. The probability distributions of these variables are adopted from Noorbala Tafti and Mahsuli [43], which proposed lognormal distributions with coefficients of variation (CoV) of 24.9% and 5.6% based on laboratory tests.

2.3. Elements and boundary conditions

The concrete part is modeled using 3D hexahedral solid elements with eight nodes, formulated based on reduced integration. A fine mesh with an approximate element size of 7 cm is adopted. The steel reinforcements are modeled using space truss elements with two nodes. Steel bars are embedded in the concrete and thus, the slippage of the bars is not considered. In fact, slippage negligibly affects the global behavior of the pole [33], which is of interest in this study. Poles with height of 9, 12, and 15 m are embedded in the ground up to the elevation of 1.40, 1.68, and 2.10 m, respectively, with no footing. Hence, to model the boundary condition of the pole, all degrees of freedom are restrained in the embedded part of poles.

2.4. Failure criteria

To model the propagation of cracks, the following two failure criteria are defined: 1) the degradation of the compressive stress by more than $\widehat{d}_c \cdot f_c'$, where $\widehat{d}_c$ is the damage parameter at the crushing strain of concrete, i.e., $\widehat{\varepsilon}_c = 0.003$, and the exceedance of the plastic compressive strain from the corresponding ultimate strain, $\widehat{\varepsilon}_c^{pl}$; 2) the degradation of the tensile stress by more than $\widehat{d}_t \cdot f_t$, where $\widehat{d}_t$ is the damage parameter at the ultimate tensile strain of concrete, and the exceedance of the plastic tensile strain from the corresponding ultimate strain, $\widehat{\varepsilon}_t^{pl}$. Failure occurs when either of these two criteria are met, which is formulated as follows:

$$\left(\left(\sigma_c \le \widehat{d}_c \cdot f_c'\right) \wedge \left(\varepsilon_c^{pl} \ge \widehat{\varepsilon}_c^{pl}\right)\right) \vee \left(\left(\sigma_t \le \widehat{d}_c \cdot f_t\right) \wedge \left(\varepsilon_t^{pl} \ge \widehat{\varepsilon}_t^{pl}\right)\right) \tag{9}$$

Upon meeting these criteria in an element, the element is omitted from the analysis to model the initiation or the propagation of a crack in the concrete in order to better visualize and determine the damage state

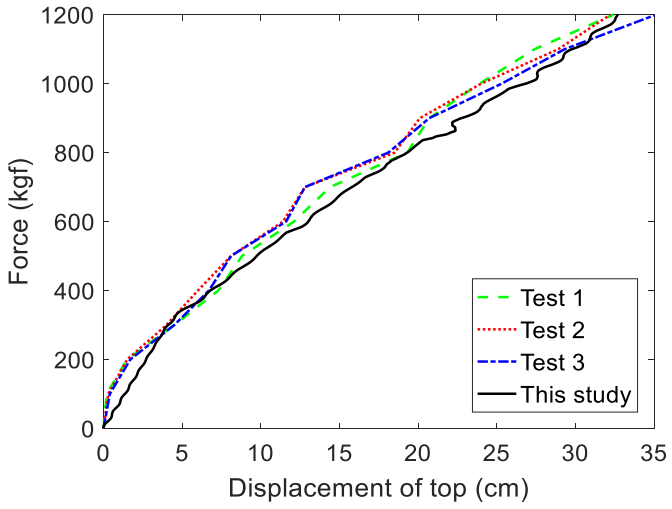

Fig. 4. Comparison between load-displacement response of simulation and experimental results in Ref. [25].

of the pole in later stages of the work on fragility analysis. According to Eqs. (3)–(6), $\widehat{d}_c = 0.18$, $\widehat{d}_t = 0.9$, $\widehat{\varepsilon}_c^{pl} = 0.0018$, and $\widehat{\varepsilon}_t^{pl} = 0.0017$.

The total collapse of the pole, which is also of interest in this study, occurs due to the instability of the pole. The considerable increase in displacement has been used as an indicator of structural instability in many past studies; see, for instance, Refs. [44–50].

2.5. Validation with experimental studies

The finite element model of 12 m-long pole is validated using experimental studies conducted by Zeynalian and Khorasgani [25]. They subjected three 12 m-long concrete poles to a monotonic load applied at 60 cm from the top of the specimens. The bottom 1.68 m of the poles was fixed using two concrete blocks. In addition, load cells and potentiometers were employed to record the load and the displacement [25]. The load was gradually applied to the specimens with a linear ramp function to minimize dynamic effects [51]. In the finite element model here, the same loading pattern is applied. Furthermore, the load is applied to a 60 cm wide surface, which is restrained to a reference point at the center with rigid body constraint to reduce stress concentration effects. The boundary conditions of the bottom are as explained in Section 2.3. The dynamic explicit analysis, which is more efficient in terms of convergence for the material behavior involving damage, is employed herein. This explicit analysis requires small time increments for stable and sufficiently accurate results. The total energy output is employed to control the correctness of results. In the explicit analyses conducted, the total energy is nearly constant over the course of each analysis with an error of less than 3%, which means the input and output energy are nearly equal. Fig. 4 compares the load-displacement relationship of the simulation with those of the tests. As seen, the results of the model developed in the present study are in close agreement with those of the tests.

The pole model is further pulled to observe the damage and failure mechanism. Fig. 5 shows the base shear versus displacement of top along with deformations and damage patterns at different displacements. Fig. 5 shows that three successive stages of failure occur, i.e., the cracking of the concrete, the yielding of longitudinal bars, and final instability, at tip displacements of 4.5, 41, and 56 cm, respectively. The

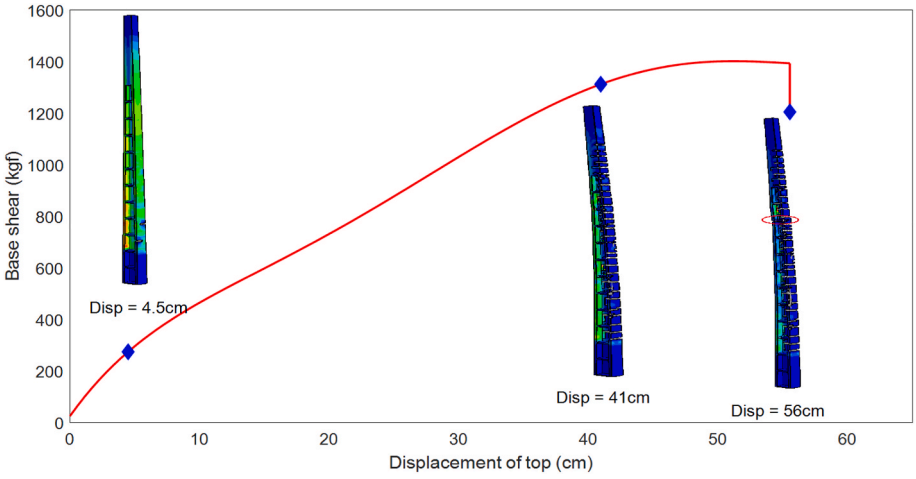

Fig. 5. Displacement of top versus base shear and deformation at certain displacements.

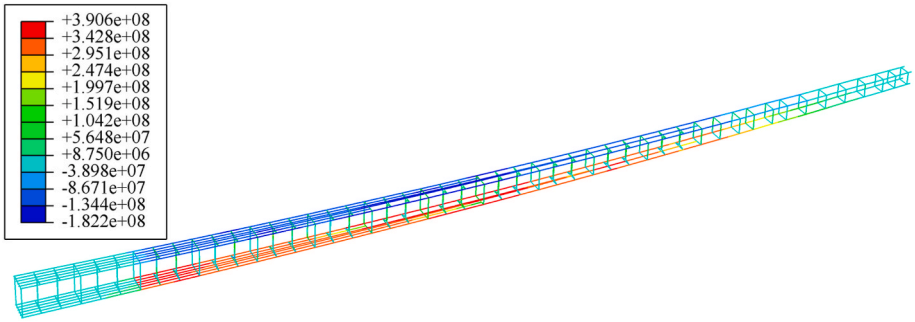

Fig. 6. Stress in rebars (Pa) at the top displacement of 41 cm.

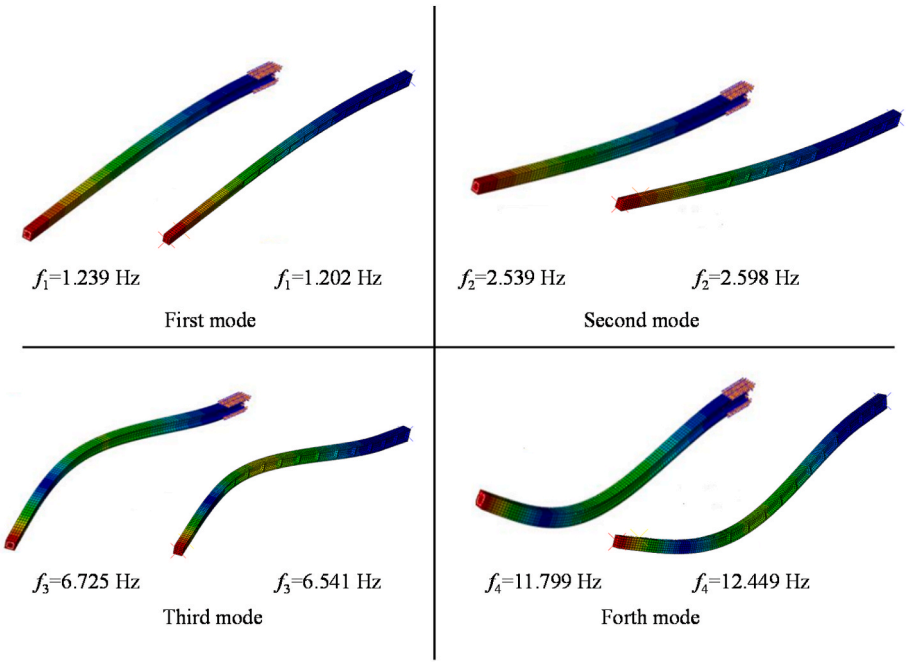

Fig. 7. Comparison of the first four natural frequencies and mode shapes obtained in the present study for the 12 m pole, shown on the right for each mode and those obtained by Ref. [25], shown on the left for each mode.

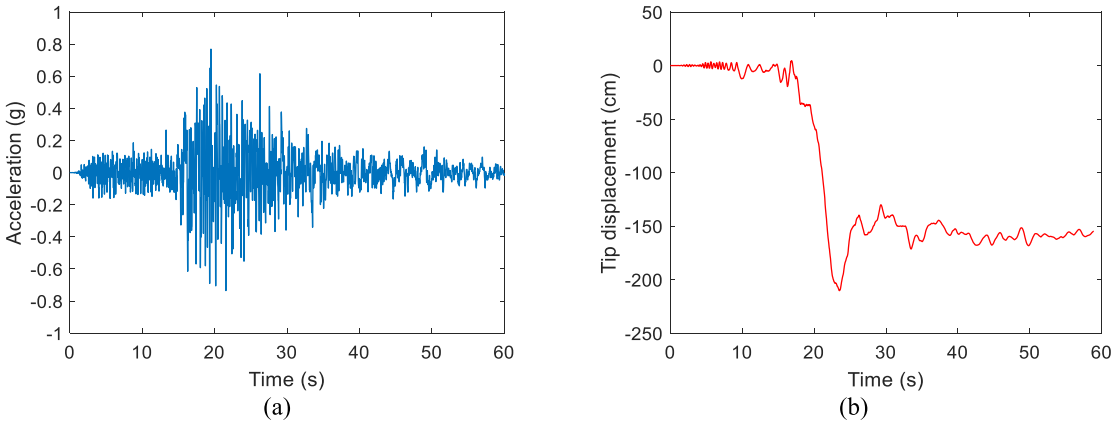

Fig. 8. (a) Acceleration time history of the 2003 Bam, Iran earthquake (b); the resulting displacement time history response at the top of the 12 m-long pole.

pole behaves linearly until the first cracks is formed in the concrete. Then, a slight softening behavior occurs, and the spalling of the cover concrete at the tension face propagates along the height. After longitudinal bars yield in tension, the displacement of the top increases while the base shear remains nearly unchanged. Primary stress contours of the reinforcing bars at the onset of yielding are shown in Fig. 6 in the units of Pa. Finally, the crushing of concrete in compression at 7.5 m from the base leads to a sudden collapse. The failure occurs at the imposed force of 1450 kgf in simulation, while the ultimate resisting force of 1500 kgf was reported in the experiment by Zeynalian and Khorasgani [25]. Thus, the error regarding the estimation of the failure load is less than 4%.

Next, dynamic properties of the structure are evaluated since they notably affect the accuracy of dynamic time history analysis. An eigen-analysis is carried out on the finite element model of the 12 m-long pole to compute natural frequencies and mode shapes of the pole model, which are then compared with those obtained by Ref. [25]. The results are shown in Fig. 7 for the first four modes. As seen, the natural frequencies and mode shapes are consistent with those provided by Zeynalian and Khorasgani [25]. The maximum deviation in the prediction of frequencies is less than 5%. Fundamental natural frequencies of the 9, 12, and 15 m poles are 1.88, 1.20, and 0.96 Hz, respectively.

2.6. *Validation with observations from past earthquakes*

A comparison between collapse patterns observed in the actual earthquakes with those in simulation reveals the accuracy of the model in predicting the final stages of damage and collapse. To this end, the acceleration time history of the ground motion in Bam 2003, Iran earthquake [3] shown in Fig. 8a is applied to the base of the 12 m-long pole model, and the displacement history of the top is recorded as depicted in Fig. 8b. It can be seen from Fig. 8b that failure is accompanied by a dramatic increase in the displacement response. Fig. 9 demonstrates the failure pattern obtained by the simulation and those observed in the actual earthquake. As seen, in both the simulation and the real earthquake, the cover concrete spalls near the ground, and the failure occurs due to a significant deflection of longitudinal bars.

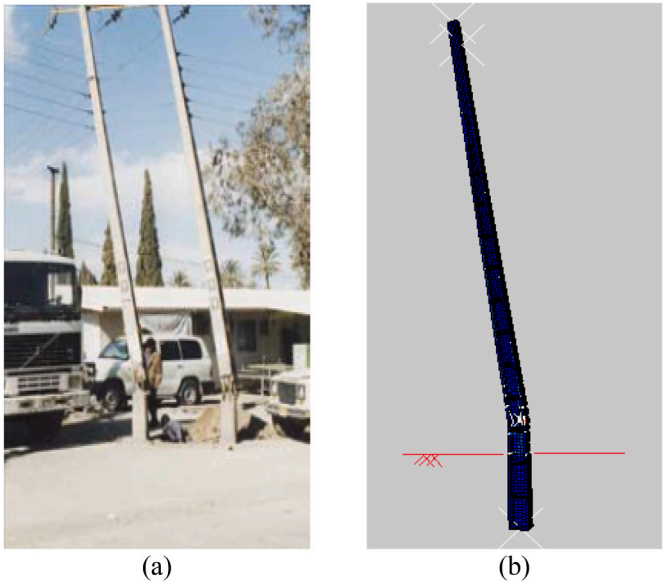

Fig. 9. Comparison of the failure of the concrete pole in (a) 2003 Bam, Iran earthquake [3] and (b) the finite element model of the present study.

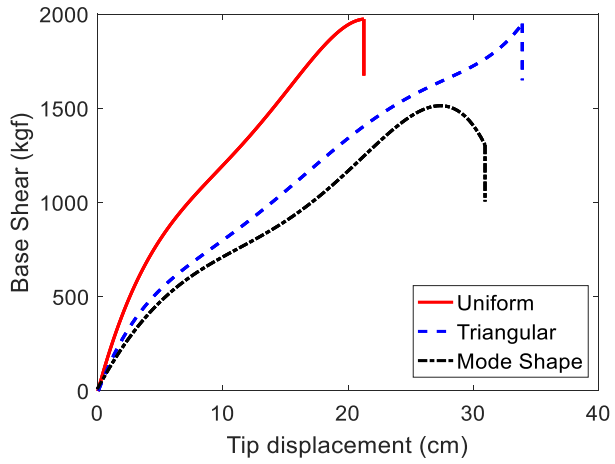

Fig. 10. Base shear versus the tip displacement curves under various loading patterns.

3. Nonlinear static analysis

Nonlinear static analysis is usually considered as an alternative for the computationally-costly time history analysis. Furthermore, effects of wind, ice, and snow loads on wires can be viewed as static load that poles encounter during their lifetime. Static pushover analysis is carried out on the 12 m-long pole in this section to determine the capacity and damage pattern of the pole under static loads and to study the effects of the loading pattern, loading direction, material strength, and failure criteria on the collapse pattern.

3.1. Sensitivity to loading pattern

To investigate the influence of the static loading pattern on the performance of the pole, three loading patterns including uniform, reversed triangular, and first-mode proportional are considered. The resultant force of each pattern is 2000 kgf. These loads are applied over the course of 20 s with a time step of 0.0001 s. Fig. 10 shows the capacity curves of the pole when different loading patterns are applied. As seen,

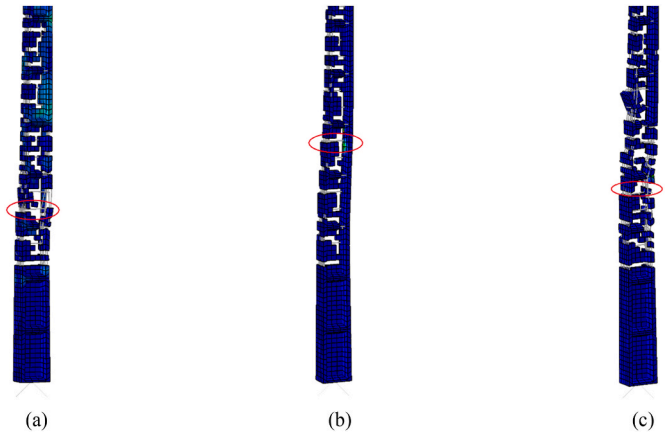

Fig. 11. Damage pattern under (a) uniform (b) triangular, and (c) mode-shape proportional load patterns.

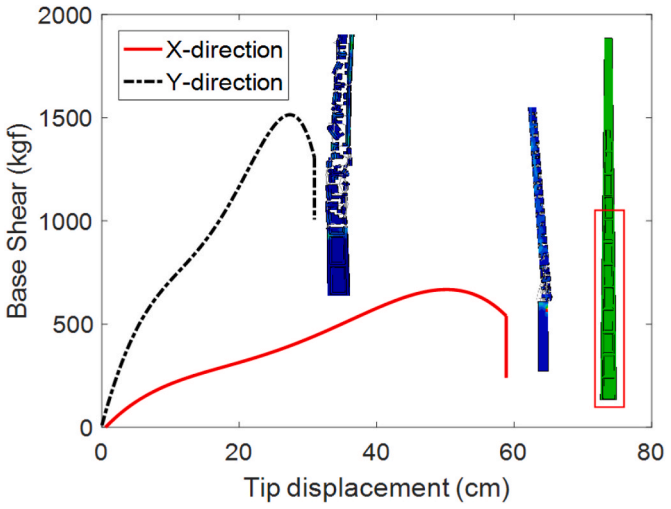

Fig. 12. Base shear versus the tip displacement and collapse patterns obtained from different loading directions.

the pole under the uniform loading pattern demonstrates a peak capacity of 2000 kgf. Nevertheless, using the triangular pattern leads to a peak displacement capacity of 33 cm. The comparison of the area under each curve indicates that the pole has the highest ductility under the triangular pattern and the lowest ductility under the uniform pattern. These observations reveal that the loading pattern has a significant influence on the capacity of poles.

The pattern of the damage incurred by the pole under different loading patterns immediately before instability is depicted in Fig. 11. Fracture initiation points are demonstrated by red ovals. Extensive spalling of concrete in the cover and web of the pole is clearly seen in all cases. However, the fracture initiated at different locations under different loading patterns. The fracture point under the uniform and mode-shape proportional loading patterns are closer to the base of the pole, similar to what the dynamic time history analyses show in Section 4.

3.2. Sensitivity to loading direction

The effects of loading directions on the performance of the pole are investigated in this section. The mode-shape proportional pattern is individually employed on the face of the pole in the x and y directions. As shown in Fig. 2, the larger face of the pole is in the y direction and the smaller face is in the x direction. Fig. 12 shows load-displacement

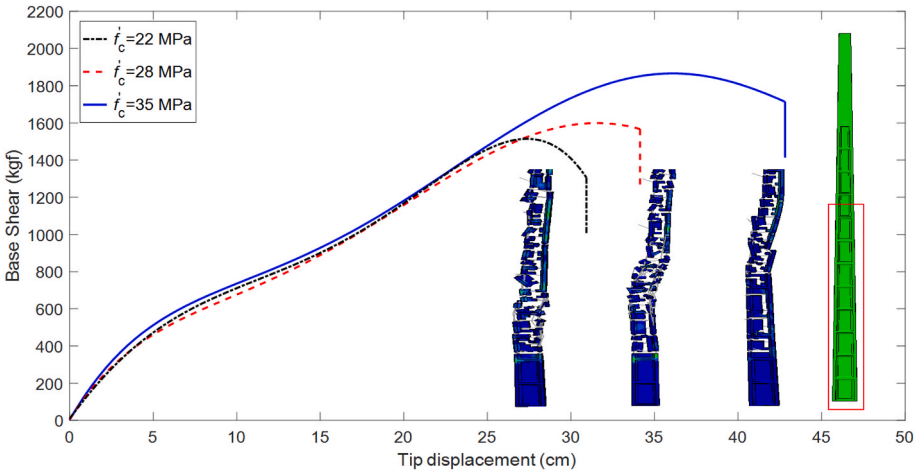

Fig. 13. Effects of various concrete strengths on the collapse pattern and on the base shear versus tip displacement response.

relationships along with damage patterns immediately before the collapse. As seen, the behavior of the pole in the x direction is more ductile than that in the y and hence, the pole is able to resist higher displacement demands. The load-bearing capacity of the pole in the y direction, however, is almost three times larger than that in the x direction. In addition, the collapse initiation location is different between the two directions. The ultimate fracture occurs at 168 and 310 cm when the pole is subjected to the load in the x and y directions, respectively. The higher displacement capacity for loading in the x direction can be attributed to the insignificant spalling of the web concrete, which emphasizes the considerable contribution of the web concrete to the performance.

3.3. Sensitivity to concrete strength

A total of three different finite element models are developed to investigate the effect of the concrete strength (f_c') on the performance of poles. Three levels of concrete strength, i.e., low, medium, and high, are employed here with f_c' values of 22, 28, and 35 MPa, respectively. The constitutive material law and failure criteria are adopted for each model in accordance with Sections 2.2 and 2.4. Then, the mode-shape proportional loading pattern is applied on these three models.

The predicted base shear versus tip displacement curves are shown in Fig. 13. In addition, damage patterns and deflections are illustrated in this figure when poles can no longer resist loading. Load-displacement curves are relatively similar up to tip displacement of nearly 25 cm, but the collapse point varies significantly among different concrete strengths. The fracture takes place at tip displacements of 30, 34, and 43 cm for low, medium and high strength concrete, respectively. In turn, the maximum capacities of specimens are 1510, 1600, and 1860 kgf for low, medium, and high strength concrete, respectively. This reveals that in the range of high-strength concrete, the pole capacity is more prominently affected by the concrete strength than in the range of low- and moderate-strength concrete. Moreover, as seen in Fig. 13, the onset of fracture for specimens with concrete strength of 22, 28, and 35 MPa is at 168, 340, and 490 cm from the base, respectively. Thus, increasing in the concrete strength leads to fracture initiation at a higher elevation. It is worth noting that extensive spalling of concrete propagated along the height is observed in all specimens before the fracture.

3.4. Sensitivity to failure criteria

Failure criteria determine when an element should be omitted from the model due to the failure of the material, as previously described in Section 2.4. To investigate the relative importance of each criterion in the total response of the pole, failure criteria are considered individually. Recall that the first criterion was defined on the exceedance of the damage parameters from the ultimate damage threshold and the exceedance of the plastic strain from its ultimate threshold in compression, and the second criterion followed similar rules in tension.

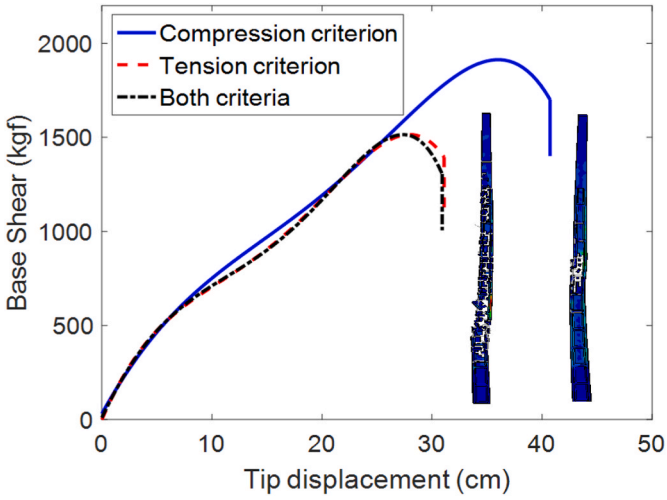

Fig. 14. Base shear versus tip displacement and the final deformation for different failure criteria.

Table 3
Summary of sensitivity analysis results.

		Ultimate disp (cm)	Max bearing capacity (kgf)	Fracture point elevation (m)
Loading pattern	Uniform	21.3	1974.4	2.25
	Triangular	33.9	1949.8	3.60
	1st mode proportional	30.9	1510.0	2.35
Loading direction	X dir	58.8	702.5	1.68
	Y dir	30.9	1510.0	3.10
Concrete strength, f_c'	22 MPa	30.0	1510.0	1.68
	28 MPa	34.0	1600.0	3.40
	35 MPa	43.0	1860.0	4.90
Failure criteria	Only tension	31.1	1512.1	3.00
	Only compression	40.7	1912.8	5.30

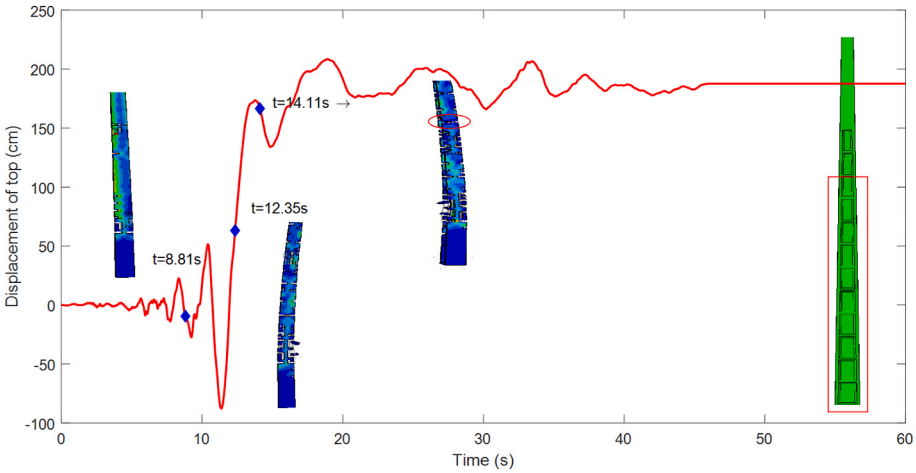

Fig. 15. Time history response at the tip of the pole and the deformed shapes and damage incurred by the pole at key time instants when the ground motion is only applied in the *x* direction.

Fig. 14 compares the load-displacement curves when these criteria are individually applied and when both are considered simultaneously in the finite element model. When only the compression criterion is applied, the final displacement and the load-bearing capacity are overestimated by 33% and 26%, respectively. However, when only the tension criterion is considered, the capacity curve is similar to that obtained considering both criteria. It can be concluded that the tension criterion has a more pronounced effect on the overall response compared to the compression criterion.

Damage patterns shown in Fig. 14 reveal that the crushing of concrete is concentrated in a limited region of the pole when only the compression criterion is considered, and the pole eventually fractures at the height of 530 cm from the base. In the case of tension criterion, cracks and spalling are observed in a wider region, and the fracture occurs at the height of 300 cm from the base.

Table 3 summarizes the results of the sensitivity analyses. In particular, this table shows how sensitive the ultimate displacement, maximum bearing capacity, and elevation of fracture initiation point are to the loading pattern, loading direction, concrete strength, and failure criteria.

4. Nonlinear dynamic analysis

This section subjects the 12 m-long pole model to a nonlinear dynamic time history analysis under ground motion records, and investigates the effect of the ground motion direction, record-to-record variability, and concrete strength on the seismic response and the collapse pattern of the pole.

4.1. Sensitivity to the direction of ground motion

The base of the pole is excited using the horizontal displacement time history of a ground motion record individually in the *x* and *y* directions to assess the sensitivity of the pole responses to the ground motion direction. For this purpose, the time history of the 1990 Manjil, Iran earthquake, with a moment magnitude of 7.4, recorded at Abbar station [52] is employed. Using an incremental dynamic analysis, the minimum peak ground acceleration (PGA) that leads to the failure of the pole in the *x* direction is estimated at 1.08 g. Fig. 15 shows the displacement history of the tip of the pole when the ground motion is scaled to reach a PGA of 1.08 g and is applied in the *x* direction. This figure also demonstrates the deformed shape and the damage incurred by the pole at a number of time instants. At 8.81 s in the record, fine cracks form near the ground, i.e., 1.68 m from the base. At 12.35 s, the deflection increases significantly to 63 cm, and cracks propagate throughout the pole. Finally, at 14.11 s, fracture initiates at the height of 575 cm from the base and the pole can no longer resist the earthquake excitation.

When the ground motion input is applied along the wider direction

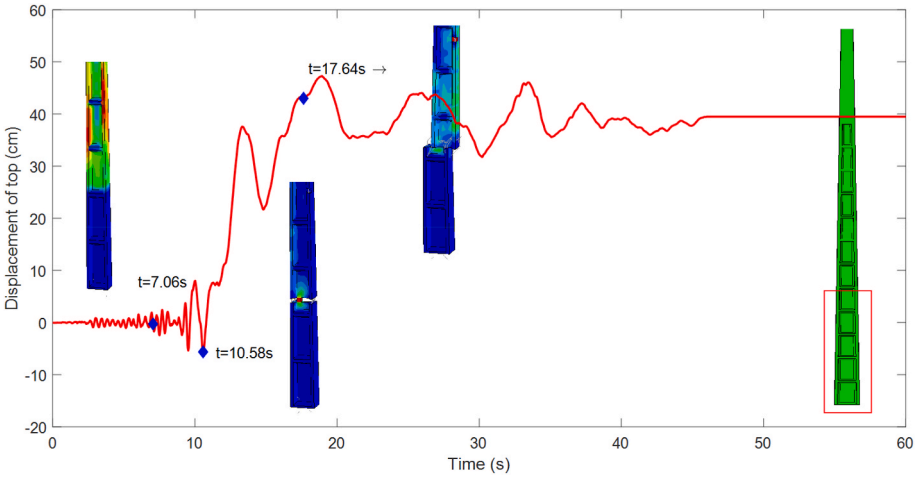

Fig. 16. Time history response at the tip of the pole and the deformed shapes and damage incurred by the pole at key time instants when the ground motion is only applied in the *y* direction.

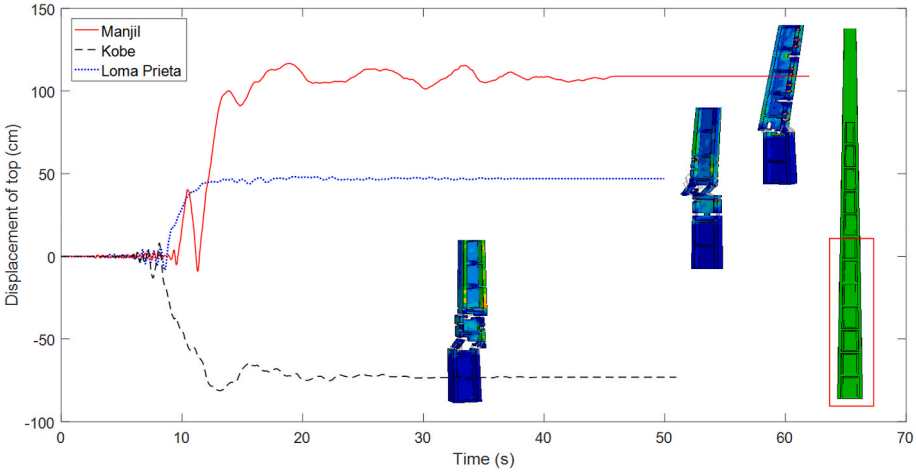

Fig. 17. Effects of record-to-record variability on the time history response and the collapse pattern of the pole.

of the pole, i.e., the *y* axis, the minimum PGA for failure is estimated at 0.38 g using another incremental dynamic analysis. The considerable discrepancy between the PGAs causing failure in the two directions may be attributed to the concentration of damage at the ground elevation of the pole when the input is in the *y* direction. Fig. 16 shows the displacement response at the tip of the pole and the damage pattern at key time instants when the ground motion is solely applied in the *y* direction. At 7.06 s, no cracks are observed, and the deformation of the pole is slight. At 10.58 s, cracks and spalling of concrete occur at the ground level, i.e., 1.68 m from the base. In addition, longitudinal bars lose their confinement. At 17.64 s, the pole experiences a large deformation in longitudinal bars, which results in the fracture of the pole at the ground level. Comparison between Figs. 15 and 16 indicates that the pole can resist tip displacements up to 170 cm before the failure in the *x* direction, which is significantly higher than the displacement of 43 cm in the *y* direction.

4.2. Record-to-record variability

To investigate the effect of record-to-record variability on the collapse pattern of the pole, three ground motion records from the Manjil earthquake, used previously, the 1995 Kobe, Japan earthquake with a moment magnitude of 6.9 [52] recorded at the Nishi-Akashi station, and the 1989 Loma Prieta, United States earthquake with a moment magnitude of 6.9 [52] recorded at the Capitola station, are employed as input. The two horizontal components from each of these ground motion records are applied simultaneously to the base of the pole. Using incremental dynamic analyses, the minimum PGA of the larger component that leads to the failure of the pole is estimated at 0.38 g, 0.58 g, and 0.28 g for the Manjil, Kobe and Loma Prieta records, respectively. The two components in each pair of these ground motions are scaled using the same scaling factor such that the PGA of the larger component coincide with the aforementioned PGA. Fig. 17 shows the time history response of the tip displacement as well as the deformed shape and the damage pattern of the pole at the failure time instant. These results reveal that the seismic collapse capacity of the pole differs significantly between various records.

As seen in Fig. 17, the fracture initiates and concentrates nearly at the ground level, i.e, 1.68 m from the base, when the pole is subjected to Manjil and Kobe ground motions. However, in the case of the Loma Prieta ground motion, the fracture occurs at 230 cm from the base. Further investigation using a suite of 44 ground motions, introduced in the next sections, reveals that even though record-to-record variability leads to different collapse patterns, the fracture under the majority of ground motions occurs within a 50 cm portion of the pole above the ground level. Thus, to increase the capacity of the pole, it is recommended that this region be strengthened, e.g., using such methods as confining with FRP wraps. Nevertheless, evaluating the influence of segmental strengthening on the performance of the pole requires more investigation in future studies.

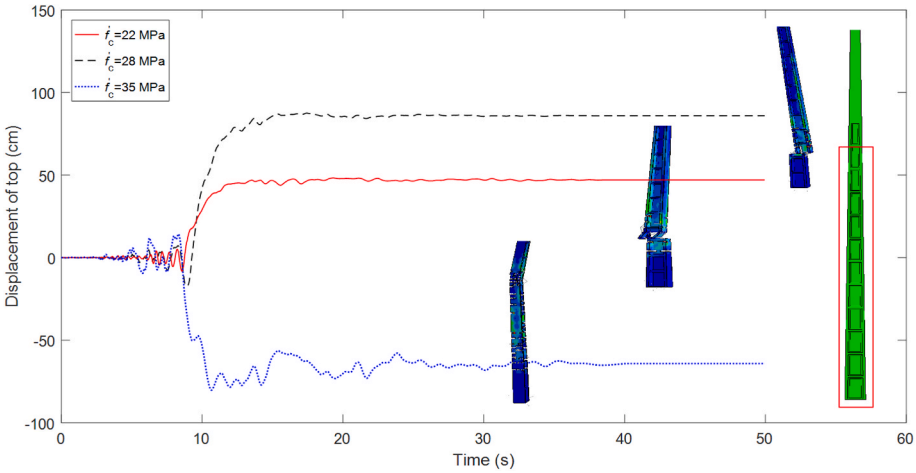

Fig. 18. Effects of the concrete strength on the response time history and the collapse pattern. The damaged shape of the pole only shows the portion indicated by a rectangle on the right of the figure.

By comparing the failure pattern of the pole under the three ground motion records in Fig. 17 with those obtained by applying a concentrated monotonic load at the top in Fig. 5, it is found that the collapse patterns under earthquake ground motions significantly differ with those under static loading. Thus, predicting the collapse pattern of poles under the earthquake excitation with simulations or laboratory experiments under monotonic concentrated forces may lead to inaccurate results.

4.3. Sensitivity to concrete strength

To investigate the effects of the compressive strength of concrete, the previously presented finite element models with various concrete strengths are here subjected to the Loma Prieta ground motion record. The minimum PGA that leads to the failure of the pole is estimated at 0.28, 0.3, and 0.58 g for specimens with a concrete strength of 22, 28 and 35 MPa, respectively, using incremental dynamic analysis. The considerably higher collapse capacity of the 35 MPa specimen indicates that high-strength concrete significantly enhances the seismic capacity of poles.

Fig. 18 illustrates displacement histories at the tip of the pole along with collapse patterns for the three specimens. It is observed that, despite widely varying displacement time histories, the collapse occurs in all specimens at around 10 s into the ground motion with a dramatic increase in the top displacement. Fig. 18 also shows that when the concrete strength is 22 MPa, the fracture occurs at the height of 230 cm from the base, accompanied by the crushing of the concrete between the elevations of 190 cm and 230 cm. When the concrete strength is 28 MPa, cracks mostly form at the lower quarter of the pole, and the fracture occurs at the ground level. When the concrete strength is 35 MPa, although several cracks are observed at the ground level, the pole eventually fractures at the height of 620 cm from the base. It is worth noting that the occurrence of fracture at higher elevations was also previously observed in the pushover analysis of the 35 MPa specimen. The above-mentioned results reveal the significant influence of the concrete strength on the collapse capacity and collapse pattern of the pole.

5. Development of fragility models

Fragility analysis is carried out to assess seismic damage and collapse probability of poles given the ground shaking intensity measure. A suite of ground motion records is selected to account for the record-to-record variability, and the incremental dynamic analysis is performed on finite element models. To account for the modeling uncertainty, each ground motion record is paired with a set of random realizations of the variables that described the uncertainty in material properties, from which a randomly generated finite element model is formed. The model is then subjected to the selected record at increasing levels of the intensity measure to complete the IDA. This procedure is repeated for other realizations of random variables. Two damage states are considered, entitled irreparability and collapse. The limit-state capacity for irreparability damage state is determined based on the residual displacement of the pole, as recommended by Ref. [53]. The collapse damage state is assumed to be associated with the global instability of the pole. The maximum likelihood method is then applied to the results of the incremental dynamic analysis to compute the median and dispersion of the fragility models. The following sections provide further details of the analyses and fragility models.

5.1. Ground motions

The suite of 22 far-field records of FEMA-P695 [52] is utilized in the incremental dynamic analysis. By switching horizontal components, a set of 44 records is obtained. Switching the horizontal components in a pair of ground motion records for further analyses in three-dimensional

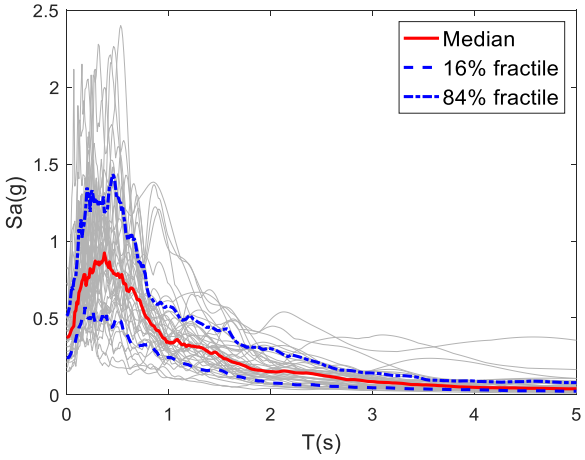

Fig. 19. Spectral acceleration of individual records.

IDA has been practiced in previous studies; see, for instance Refs. [54, 55], among others. In order to compute the residual displacement, a free vibration with duration of 10 s is added to the end of each record. As seen in Fig. 18, this extra 10 s provides ample time for the free vibration to die out so that the residual displacement can be accurately calculated. Response spectra of the 44 individual records with a 5% damping are shown in Fig. 19 along with the 16%, 50% and 84% percentiles.

5.2. Incremental dynamic analysis

Incremental dynamic analysis developed by Ref. [19] is used to quantify responses at different earthquake shaking intensities. First, PGA, which is a common intensity measure for the components of the power infrastructure [11,56,57], is employed herein. Next, the spectral acceleration at the fundamental period of vibration, $S_a(T_1)$, is considered as an alternative intensity measure to explore which IM leads to a less uncertainty in the prediction of responses. The IDA involves a multitude of three-dimensional analyses in which the finite element model is simultaneously subjected to a pair of horizontal components of a ground motion record. The two components in a pair of horizontal ground motion are indeed scaled using the same scaling factor such that the larger component coincides with the desired IM value. As such, the ratio of the two components remains unchanged after scaling. The scaling of each pair starts at an IM value of 0.05 g. The records are then scaled up with steps of 0.1 g until the global instability is reached. The maximum displacement and the residual displacement of the tip of the pole are recorded as response parameters at each IM level. Fig. 20a demonstrates the maximum tip displacement of the 12 m-long pole for individual records versus the maximum PGA of the two components. The points of global instability are indicated by red diamonds in this figure. As seen, failure leads to a dramatic increase in the displacement response. PGAs at which the global instability occurs are widely dispersed in the range of 0.2–0.8 g, which illustrates the significant effect of the record-to-record variability on the collapse capacity of poles. In comparison, Fig. 20b demonstrates the maximum tip displacement versus $S_a(T_1)$. Comparing the ensemble of IDA curves in Parts a and b of Fig. 20 reveals a smaller dispersion when $S_a(T_1)$ is employed. Hence, $S_a(T_1)$ is employed in this paper to generate the fragility curves of poles. A comparison will be made later in this paper between the resulting fragility curves for the two intensity measures, which reveals a lower uncertainty when $S_a(T_1)$ is employed.

At this point, using the spectral acceleration as the intensity measure, the IDA is conducted on the pole models of various heights while accounting for the material uncertainty. Fig. 21 demonstrates the resulting maximum displacement of the poles versus the maximum $S_a(T_1)$ of two

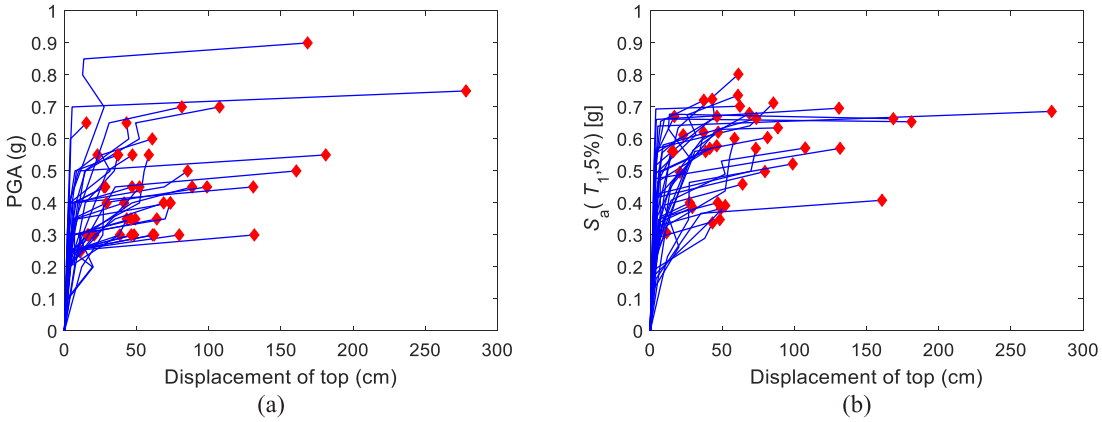

Fig. 20. Tip maximum displacement versus (a) PGA and (b) $S_a(T_1)$ for the 12 m-long pole.

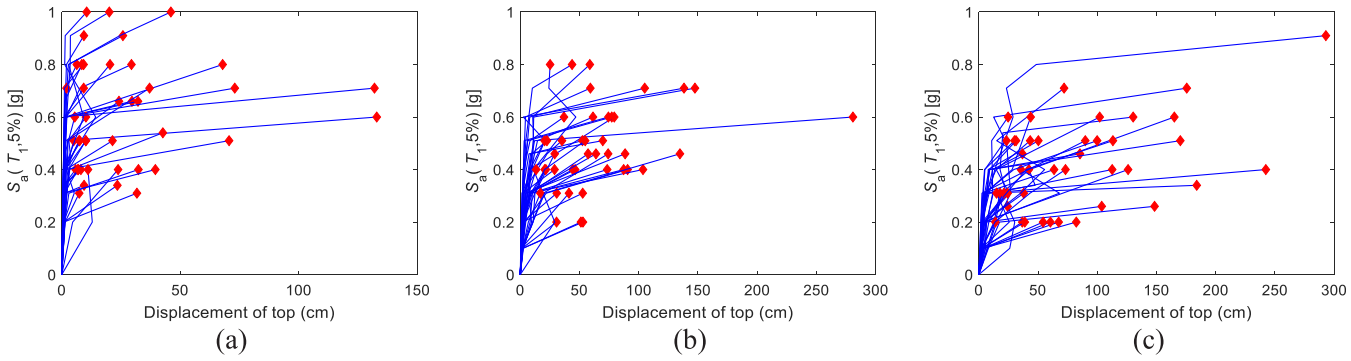

Fig. 21. Tip maximum displacement versus $S_a(T_1)$ for the (a) 9 m-long, (b) 12 m-long, and (c) 15 m-long poles.

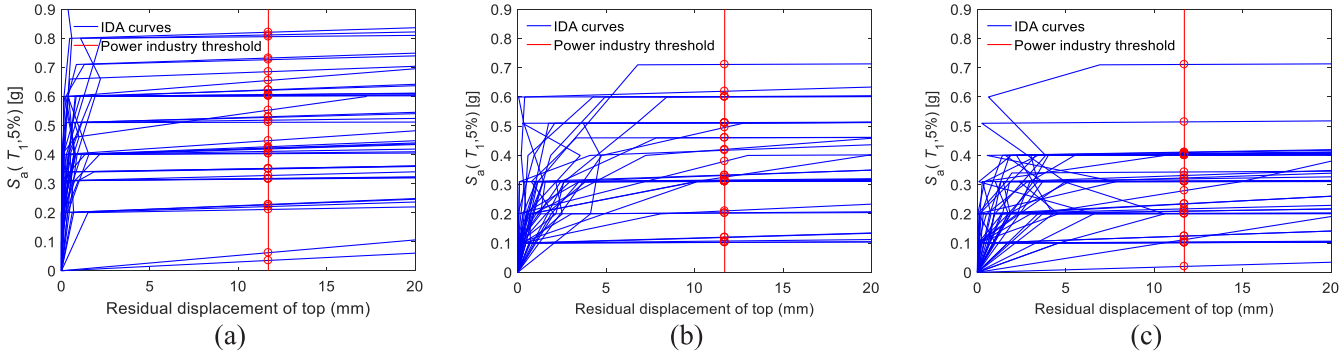

Fig. 22. Tip Residual displacement versus $S_a(T_1)$ for the (a) 9 m-long, (b) 12 m-long, and (c) 15 m-long poles.

ground motion components for various pole types. It should be noted that the nonlinear dynamic analysis of the developed model is computationally costly, and the IDA analysis took 110 days to be completed using parallel computing on a machine with 12 cores. As such, the number of records was limited to 44 in this analysis. The IMs corresponding to the global instability are utilized in the next section to develop the fragility curve for the collapse damage state.

Fig. 22 shows the tip residual displacement of poles versus the intensity measure for each record. The displacement that dies out after the free vibration is considered as the residual displacement; see Fig. 18 for instance. Fig. 22 also demonstrates the threshold on the residual displacement that defines the irreparability damage state. This threshold is determined based on the fact that the Iranian standard for concrete power poles [53] prescribes the replacement of a pole when it endures a tip residual displacement of 10% of the elastic displacement. For the type of poles considered herein, the elastic displacement corresponds to a force of 600 kgf in the pull test [53]. This force corresponds to a tip elastic displacement of 120 mm per Fig. 4. Therefore, the irreparability threshold is assumed 12 mm. For each record, the IM that leads to a residual displacement of 12 mm is indicated with a circle in Fig. 22. These IMs are utilized in the next section to develop the fragility curve of the irreparability damage state.

5.3. Fragility models

The two damage states modeled here are the irreparability and

Table 4
Parameters of fragility models of various poles for the two damage states.

	Irreparability		Collapse	
	Median (g)	Dispersion	Median (g)	Dispersion
9 m-long pole	0.441	0.523	0.569	0.375
12 m-long pole	0.330	0.547	0.462	0.353
15 m-long pole	0.256	0.639	0.386	0.453

collapse. The former state does not disrupt the functionality of the pole immediately but may cause casualty and prompts for the replacement of the pole since the repair of the pole in this damage state is costlier. The latter state, i.e., collapse, is associated with the fracture of the pole leading to lack of stability and resistance to further displacements. The major difference between these two damage states is in their impact on the grid functionality after an earthquake and thus, on indirect losses. The collapse damage state interrupts the grid functionality immediately after an earthquake, resulting in an interruption in the emergency response and recovery and inflicting business interruption losses. On the other hand, the irreparability damage state does not cause an interruption in the grid performance immediately after an earthquake.

The probability of falling in, or exceeding, a damage state given the intensity measure is described by fragility models. Fragility models are commonly defined by a lognormal cumulative distribution function [58–63]. Estimating the fragility parameters, i.e., the median, θ, and the dispersion, β, is a statistical procedure. Two methods are commonly employed in the literature to estimate these parameters. First is the computation of the second moments of the natural logarithm *IM* at the onset of the damage state under consideration, i.e., the mean and the standard deviation of the ln(*IM*). The second, more robust method is the maximum likelihood method, which is employed here to estimate the fragility parameters. In this method, the likelihood of observations, here, the data simulated using IDA, is maximized by finding the optimal values for the median and the dispersion of the fragility curves. Detailed descriptions and relationships of this method can be found in Baker [58]. The medians and dispersions of the two irreparability and collapse damage states of poles obtained through this method are listed in Table 4. The results indicate that the vulnerability of concrete poles increases with their height. The resulting fragility curves are plotted in Fig. 23 along with the data points. This figure indicates the close agreement of the data with the proposed fragility models. The proposed models are immediately applicable in the seismic risk analysis of power distribution networks and seismic resilience assessment of electrified communities.

Attention is now turned to the effect of the choice of the intensity measure between PGA and the spectral acceleration, the uncertainty in material properties, and the site class on the resulting fragility curves. The resulting fragility curves of the 12-m long pole for the two IMs are compared in Fig. 24. To better compare the two, each fragility curve is normalized by its median. As seen, the selection of $S_a(T_1)$ as the intensity measure markedly reduces the uncertainty of collapse prediction, which is evident from the sharper rise of the fragility curve based on $S_a(T_1)$. In fact, the dispersion of the fragility curve based on PGA is 0.36 and that of $S_a(T_1)$ is 0.20. That is, the dispersion is reduced by 45% simply by using $S_a(T_1)$ as the intensity measure. Hence, $S_a(T_1)$ is employed in this study

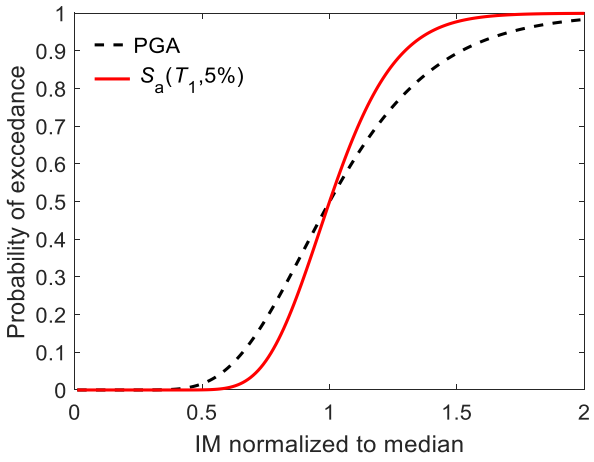

Fig. 24. Comparison between the collapse fragility of the 12 m-long pole based on PGA and $S_a(T_1)$.

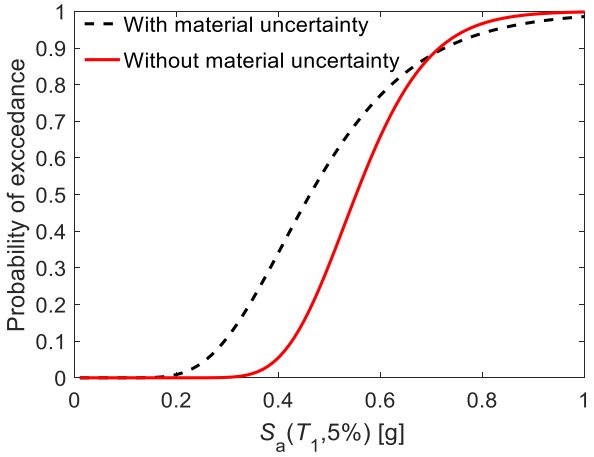

Fig. 25. Comparison between the collapse fragility of the deterministic and probabilistic model of the 12 m-long pole.

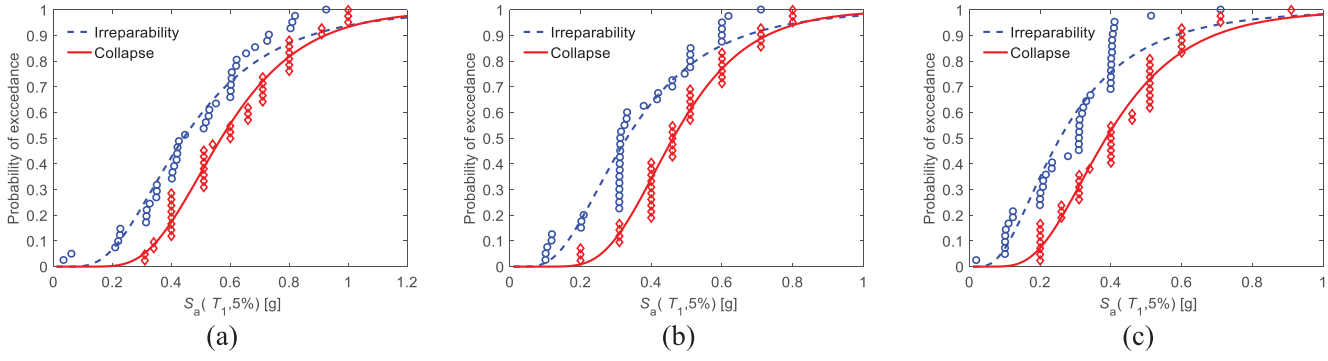

Fig. 23. Fragility curves for (a) the 9 m-long, (b) 12 m-long, and (c) 15 m-long poles.

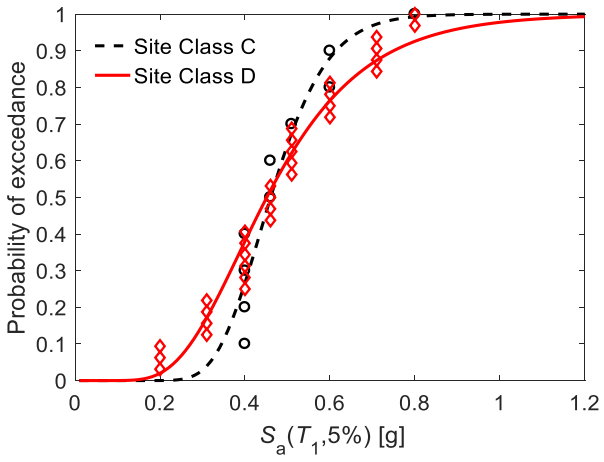

Fig. 26. Comparison between the collapse fragility of the 12 m-long pole on Site Class C and D.

to generate the fragility curves of poles.

To examine the effect of the uncertainty in material properties, the fragility curves obtained using the deterministic finite element model of the 12 m pole are compared with those obtained by accounting for the model uncertainty. The comparison is demonstrated in Fig. 25, which expectedly demonstrates a more flattened fragility curve with more uncertainty, i.e., with a less steep slope, when the model uncertainty is taken into account. In numerical terms, accounting for the material uncertainty reduces the median of the collapse fragility by 19.6% and increases the dispersion by 42.7%.

To illustrate the effect of the site class on the fragility models, fragility curves are produced individually for Site Classes C and D per ASCE/SEI 7–16 [64]. Ground motions recorded on Site Class C and D are employed separately to generate fragility models using the 44 ground motion records of FEMA P-695 [52] that are employed in this study. In particular, 12 ground motions recorded on Site Class C and 32 ground motions recorded on Site Class D are separately utilized to produce the collapse fragility curves of the 12 m-long pole, which are demonstrated in Fig. 26. The medians of the two fragility curves differ merely by 2% whereas their dispersions differ by 43%. That is, the dispersion of the fragility for Site Class C is 43% smaller than that of Site Class D. The primary reason is the lower number of records on Site Class C (12) compared to those on Site Class D (32), which has led to underestimating the dispersion in the former case.

6. Conclusions

This paper presents a comprehensive modeling and assessment of the seismic behavior of power distribution concrete poles. To this end, first a detailed finite element model of the pole is developed and verified using the results of past experimental studies and observations made in previous earthquakes. The finite element model is subjected to a sensitivity analysis with respect to the compressive strength of the concrete, record-to-record variability, direction of the ground motion, loading pattern, loading direction, and failure criteria. The finite element modeling, its verification, and the ensuing sensitivity analysis provide the following insights into the seismic behavior of concrete poles:

- The pole is most vulnerable when lateral loads are applied in the direction perpendicular to the smaller dimension of the cross-section owing to the concentration of damage at a limited region along the pole and the spalling of the web concrete.
- The damage pattern under a concentrated load that is exerted at the upper portion of the pole differs significantly from those observed under the earthquake excitation. As such, static pull tests poorly represent the seismic collapse pattern of the pole.
- The record-to-record variability leads to significantly different seismic collapse capacities under different ground motion records. However, the majority of records induce fracture within a 50 cm portion of the pole above the ground level. This yields insights into the most vulnerable segment of the pole and can guide future retrofit practices.

The verified finite element models of the poles are then employed in incremental dynamic analysis to develop damage and collapse fragility models. The resulting fragility models indicate that the vulnerability of concrete poles increases with their height. Furthermore, the effect of the uncertainty in material properties, the choice of the intensity measure between PGA and the spectral acceleration, and the site class on the resulting fragility curves are investigated. The proposed fragility models are presented in this paper for the first time and make it possible to account for the damage incurred by the power distribution lines in the seismic risk analysis of the power distribution networks as well as the seismic resilience analysis of electrified communities.

A power distribution network comprises many interconnected poles. Hence, the seismic risk of the network depends on the performance of the entire system, and not on the damage incurred by an individual pole. Damage to one pole may not necessarily lead to an interruption in the network, e.g., when the pole is in the irreparability damage state, or when the connections to adjacent undamaged poles keep the damaged pole in its position. Future research needs to address the interaction between adjacent poles and its effect on the functionality of the network.

CRediT authorship contribution statement

Amir Ghahremani Baghmisheh: Conceptualization, Methodology, Validation, Formal analysis, Visualization, Writing – original draft, preparation. **Mojtaba Mahsuli:** Conceptualization, Methodology, Validation, Supervision, Writing – review & editing.

Declaration of competing interest

The authors declare that they have no known competing financial interests or personal relationships that could have appeared to influence the work reported in this paper.

Acknowledgments

The authors thank Sharif University of Technology for Grant No. QA990102. The authors express their gratitude to Dr. Amir Safdarian from Sharif University of Technology for insightful comments on the serviceability of power poles under various damage scenarios.

References

[1] Dittmar F, Bahous H. Spun prestressed concrete poles: alternative to wooden and steel poles for low, medium, and high voltage. In: Proc. 21st int. Conf. Electr. Distrib. (CIRED 2011); 2011. p. 6–9. Frankfurt, Ger.
[2] Henin E, Morcous G, Tadros MK. Design, fabrication, and construction of static-cast concrete Poles reinforced with GFRP. Pract Period Struct Des Construct 2017;22:4017007.
[3] Zekavati A, Jafari MA, Rahnavard A, Yavartalab A, Samadi M. Development of seismic capacity curve (SCC) for power distribution concrete poles. 2013.
[4] Takada S, Bastami M, Kuwata Y, Javanbarg MB. Performance of electric power systems during the Bam earthquake and its fragility analyses. Mem Constr Eng Res Inst 2004;46:152–61.
[5] Nasrazadani H, Mahsuli M. Probabilistic framework for evaluating community resilience: integration of risk models and agent-based simulation. J Struct Eng 2020;146:4020250.
[6] Mahsuli M, Haukaas T. Seismic risk analysis with reliability methods , part I : Models. Struct Saf 2013;42:54–62. https://doi.org/10.1016/j.strusafe.2013.01.003.
[7] Mahsuli M, Haukaas T. Seismic risk analysis with reliability methods, part II: Methods. Struct Saf 2013;42:54–62.

[8] Goda K, Zhang L, Tesfamariam S. Portfolio seismic loss estimation and risk-based critical scenarios for residential wooden houses in victoria, British columbia, and Canada. Risk Anal 2020.
[9] Zhang L, Goda K, Werner MJ, Tesfamariam S. Spatiotemporal seismic hazard and risk assessment of M9. 0 megathrust earthquake sequences of wood-frame houses in Victoria, British Columbia, Canada. Earthq Eng Struct Dynam 2020.
[10] Gilani ASJ, Whittaker AS, Fenves GL, Chen CH, Ho H, Fujisaki E. Seismic evaluation and analysis of 230-kV disconnect switches. Pacific earthquake engineering research center, report 2000/06. PEER. Univ Calif Berkeley; 2000.
[11] Baghmisheh AG, Estekanchi HE. Effects of rigid bus conductors on seismic fragility of electrical substation equipment. Soil Dynam Earthq Eng 2019;125:105733.
[12] Ghahremani Baghmisheh A, Estekanchi H. Influence of dynamic interaction between interconnected electrical substation equipment on seismic response. J Struct Constr Eng 2020. https://doi.org/10.22065/jsce.2020.171843.1784.
[13] Zareei SA, Hosseini M, Ghafory-Ashtiany M. Evaluation of power substation equipment seismic vulnerability by multivariate fragility analysis: a case study on a 420 kV circuit breaker. Soil Dynam Earthq Eng 2017;92:79–94. https://doi.org/10.1016/j.soildyn.2016.09.026.
[14] Mohammadpour SHM. Experimental system identification of a 63kV substation post insulator and developing its fragility curves by dynamic finite element analyses. Earthq Spectra 2017;33:1149–72.
[15] Jaigirdar MA. Seismic fragility and risk analysis of electric power substations. 2005.
[16] Paolacci F, Giannini R, Alessandri S, De Felice G. Seismic vulnerability assessment of a high voltage disconnect switch. Soil Dynam Earthq Eng 2014;67:198–207. https://doi.org/10.1016/j.soildyn.2014.09.014.
[17] Siraj T, Tesfamariam S, Duenas-Osorio L. Seismic risk assessment of high-voltage transformers using Bayesian belief networks. Struct Infrastruct Eng 2015;11:929–43.
[18] Baghmisheh AG, Estekanchi HE. Quantifying seismic response uncertainty of electrical substation structures using endurance time method. Structures, vol. 30. Elsevier; 2021. p. 838–49.
[19] Vamvatsikos D, Cornell CA. Incremental dynamic analysis. Earthq Eng Struct Dynam 2002;31:491–514.
[20] Saafi M, Asa E. Extending the service life of electric distribution and transmission wooden poles using a wet layup FRP composite strengthening system. J Perform Constr Facil 2010;24:409–16.
[21] Vivek B, Sharma S, Raychowdhury P, Ray-Chaudhri S. A study on failure mechanism of self-supported electric poles through full-scale field testing. Eng Fail Anal 2017;77:102–17.
[22] Kliukas R, Daniunas A, Gribniak V, Lukoseviciene O, Vanagas E, Patapavicius A. Half a century of reinforced concrete electric poles maintenance: inspection, field-testing, and performance assessment. Struct Infrastruct Eng 2018;14:1221–32.
[23] Argo M. Seismic performance of aging prestressed transmission Pole with simulated. Soil Foundation. Oregon State; 2016.
[24] Saboori B, Khalili SMR. Static analysis of tapered FRP transmission poles using finite element method. Finite Elem Anal Des 2011;47:247–55.
[25] Zeynalian M, Khorasgani MZ. Structural performance of concrete poles used in electric power distribution network. Arch Civ Mech Eng 2018;18:863–76.
[26] Sun L, Stojadinovic B, Sansavini G. Agent-based recovery model for seismic resilience evaluation of electrified communities. Risk Anal 2019;39:1597–614.
[27] Didier M, Esposito S, Stojadinovic B. Probabilistic seismic resilience analysis of an electric power supply system using the Re-CoDeS resilience quantification framework. 12th Int. Conf. Struct. Saf. Reliab. ICOSSAR 2017.
[28] Liu X, Hou K, Jia H, Zhao J, Mili L, Mu Y, et al. A resilience assessment approach for power system from perspectives of system and component levels. Int J Electr Power Energy Syst 2020;118:105837.
[29] Azzolin A, Dueñas-Osorio L, Cadini F, Zio E. Electrical and topological drivers of the cascading failure dynamics in power transmission networks. Reliab Eng Syst Saf 2018;175:196–206.
[30] Mensah AF, Dueñas-Osorio L. Efficient resilience assessment framework for electric power systems affected by hurricane events. J Struct Eng 2016;142:C4015013.
[31] Ouyang M, Dueñas-Osorio L, Min X. A three-stage resilience analysis framework for urban infrastructure systems. Struct Saf 2012;36:23–31.
[32] Systemes D. ABAQUS/standard user's manual. 2014.
[33] Li C, Hao H, Bi K. Numerical study on the seismic performance of precast segmental concrete columns under cyclic loading. Eng Struct 2017;148:373–86.
[34] Lee J, Fenves GL. Plastic-damage model for cyclic loading of concrete structures. J Eng Mech 1998;124:892–900.
[35] Nguyen T, Ghazlan A, Nguyen T, Thai H-T, Ngo T. Uncertainty quantification of the mechanical properties of lightweight concrete using micromechanical modelling. Int J Mech Sci 2020;173:105468.
[36] Al Abadi H, Paton-Cole V, Patel VI, Thai H-T. Axial strength and elastic stiffness behaviour of partially confined concrete columns. Construct Build Mater 2019;196:727–41.
[37] Li C, Li H-N, Hao H, Bi K, Chen B. Seismic fragility analyses of sea-crossing cable-stayed bridges subjected to multi-support ground motions on offshore sites. Eng Struct 2018;165:441–56.
[38] Arabzadeh A, Hizaji R, Yang TY. Experimentally studying and development of curved STM to predict the load capacity and failure mode of fixed-ended RC deep beams. Structure 2020;23:289–303. Elsevier.
[39] Fang C, Mohamed Ali MS, Sheikh AH, Singh M. Numerical and finite-element analysis of short ultrahigh-performance fiber-reinforced concrete columns. J Struct Eng 2019;145:4019111.
[40] Hognestad E, Hanson NW, McHenry D. Concrete stress distribution in ultimate strength design. J. Proc. 1955;52:455–80.
[41] Vecchio FJ, Shim W. Experimental and analytical reexamination of classic concrete beam tests. J Struct Eng 2004;130:460–9.
[42] Wahalathantri BL, Thambiratnam DP, Chan THT, Fawzia S. A material model for flexural crack simulation in reinforced concrete elements using ABAQUS. In: Proc. first Int. Conf. Eng. Des. Dev. built Environ. Sustain. wellbeing. Queensland University of Technology; 2011. p. 260–4.
[43] Noorbala Tafti HR, Mahsuli M. Probabilsitic models for the yield strength of reinforcing bars and the compressive styrength of concrete based on Bayesian linear regression, Technical Report. Center for Infrastructure Sustainability and Resilience Research, Department of Civil Engine; 2020.
[44] Zhang Y, Dias-da-Costa D. Seismic vulnerability of multi-span continuous girder bridges with steel fibre reinforced concrete columns. Eng Struct 2017;150:451–64.
[45] Hoult R, Goldsworthy H, Lumantarna E. Fragility functions for RC shear wall buildings in Australia. Earthq Spectra 2019;35:333–60.
[46] Baradaran Shoraka M, Yang TY, Elwood KJ. Seismic loss estimation of non-ductile reinforced concrete buildings. Earthq Eng Struct Dynam 2013;42:297–310.
[47] Amirsardari A, Lumantarna E, Rajeev P, Goldsworthy HM. Seismic fragility assessment of non-ductile reinforced concrete buildings in Australia. J Earthq Eng 2020:1–35.
[48] Rajeev P, Tesfamariam S. Seismic fragilities of non-ductile reinforced concrete frames with consideration of soil structure interaction. Soil Dynam Earthq Eng 2012;40:78–86.
[49] Salami MR, Kashani MM, Goda K. Influence of advanced structural modeling technique, mainshock-aftershock sequences, and ground-motion types on seismic fragility of low-rise RC structures. Soil Dynam Earthq Eng 2019;117:263–79.
[50] Muho EV, Qian J, Beskos DE. Modal behavior factors for the performance-based seismic design of R/C wall-frame dual systems and infilled-MRFs. Soil Dynam Earthq Eng 2020;129.
[51] Earij A, Alfano G, Cashell K, Zhou X. Nonlinear three–dimensional finite–element modelling of reinforced–concrete beams: computational challenges and experimental validation. Eng Fail Anal 2017;82:92–115.
[52] Al K et, Fema P695. Quantification of building seismic performance factors. Washington, DC: Fed Emerg Manag Agency; 2009. https://doi.org/10.1016/j.compstruc.2009.08.001.
[53] Requirement of qualification tests for reinforeced concrete power poles. Power Distribution Organization; n.d.
[54] Leng J, Schafer BW, Buonopane SG. Modeling the seismic response of cold-formed steel framed buildings: model development for the CFS-NEES building. Proc. Annu. Stab. Conf. Missouri, Citeseer 2013.
[55] Wang Y, Rosowsky DV. Effects of earthquake ground motion selection and scaling method on performance-based engineering of wood-frame structures. J Struct Eng 2014;140:4014086.
[56] Yang SC, Liu TJ, Hong HP. Reliability of tower and tower-line systems under spatiotemporally varying wind or earthquake. Loads 2017;143:1–13. https://doi.org/10.1061/(ASCE)ST.1943-541X.0001835.
[57] Zheng H-D, Fan J, Long X-H. Analysis of the seismic collapse of a high-rise power transmission tower structure. J Constr Steel Res 2017;134:180–93.
[58] Baker JW. Efficient analytical fragility function fitting using dynamic structural analysis. Earthq Spectra 2015;31:579–99. https://doi.org/10.1193/021113EQS025M.
[59] Yue J, Qian J, Beskos DE. A generalized multi-level seismic damage model for RC framed structures. Soil Dynam Earthq Eng 2016;80:25–39.
[60] Goda K, Yoshikawa H. Incremental dynamic analysis of wood-frame houses in Canada: effects of dominant earthquake scenarios on seismic fragility. Soil Dynam Earthq Eng 2013;48:1–14.
[61] Tesfamariam S, Goda K, Mondal G. Seismic vulnerability of reinforced concrete frame with unreinforced masonry infill due to main shock–aftershock earthquake sequences. Earthq Spectra 2015;31:1427–49.
[62] Yang TY, Neitsch J, Al-Janabi MAQ, Tung DP. Seismic performance of eccentrically braced frames designed by the conventional and equivalent energy procedures. Soil Dynam Earthq Eng 2020;139:106322.
[63] Skalomenos KA, Hatzigeorgiou GD, Beskos DE. Modeling level selection for seismic analysis of concrete-filled steel tube/moment-resisting frames by using fragility curves. Earthq Eng Struct Dynam 2015;44:199–220.
[64] ASCE/SEI 7-16. Minimum design loads and associated criteria for buildings and other structures. American Society of Civil Engineers; 2017.